International Journal of Applied Electromagnetics and Mechanics 50 (2016) 367–377
DOI 10.3233/JAE-150027
IOS Press

Analytical model of magnetic field distribution in the air-gap of quartz flexible accelerometer

Cuo Wang[a,*], Xingfei Li[a], Ke Kou[a], Tengfei Wu[a] and Chunguo Long[b]
[a]*State Key Laboratory of Precision Measuring Technology and Instruments, Tianjin University, Tianjin, China*
[b]*No. 707 Research Institute of CSIC, Tianjin, China*

Abstract. As common high precision inertial sensors, quartz flexible accelerometers have wide application prospect in many circumstances such as low cost inertial navigation systems. In order to quickly evaluate magnetic field distribution in air-gap of these accelerometers and provide an insightful knowledge for design optimization, we introduced an analytical method based on scalar magnetic potential to describe their magnetic behaviour. Some related Laplace and Poison equations are solved by separating variables and the parameters of the solutions are calculated by a set of linear vector equations considering boundary conditions. Magnetic field computed with the proposed analytical method is proved effective through finite element method and some preliminary experiments, additionally, the scale factor estimated can be validated by the gravitational field roll-over test.

Keywords: Quartz flexible accelerometer, analytical model, magnetic flux density

1. Introduction

The quartz flexible accelerometer (QFA) is extensively used in inertial navigation systems, navigation orientation system, attitude and heading reference system and orientation system of oil drilling, etc., for its excellent bias, scale factor and axis alignment stability [1–4], and its performance directly affects the measurement accuracy and stability of systems [5]. As a force rebalance accelerometer [6], an important part of the QFA is the permanent magnet (PM) torquer, which is used to force the proof mass back to the null position along the sensitive axis [7]. So the QFA is also a magneto-electric feedback transducer, which can have its equilibrium position attained automatically to get higher precision and wider measuring range [8].The PM torquer include magnets, pole pieces, iron yokes and torque coils. Particularly the coils are concentrically located in the air-gap where the magnetic field is supplied by the magnetic return path [9]. The detailed knowledge of the magnetic field distribution in air-gap helps to evaluate the rebalance performance and further determines the precision, thus it is vitally important for design and optimization of QFAs [10]. However, recent research of QFA mainly focuses on temperature

*Corresponding author: Cuo Wang, State Key Laboratory of Precision Measuring Technology and Instruments, Tianjin University, Tianjin 300072, China. E-mail: wangcuo@tju.edu.cn.

compensation [11,12], parameter drift [13], signal de-noising [14] and residual stress [15], lacking sufficient concern about the magnetic field. So in this study, we propose an analytical model to discuss the magnetic field distribution in the air-gap of the QFA.

The air-gap magnetic field in the QFA can be calculated with the magnetic circuit analysis method and finite elements method (FEM). Both methods provide theory basis for designing the PM torquer. However, the magnetic circuit analysis method can not consider the slotting effects and the FEM is not only consuming long time but also poorly flexible for design [16–18]. In order to ensure the force along the sensitive axis, there is a slot in the iron yoke because the sensitive axis do not pass through the geometric center of the QFA. So the PM torquer does not have a sufficient symmetry structure to adopt the magnetic circuit analysis method [19–21]. Fortunately, the air-gap magnetic field with slotting effects can be evaluated by several techniques including analytical and semi-analytical methods, which are often used in the analysis of PM motors [22–26] and PM bearings [27,28].

Here, an analytical technique named sub-domain method is introduced to calculate the magnetic field distribution in the air-gap of the QFA's torquer for the method can provide an insightful knowledge for design. The method uses a set of partial differential equations in terms of scalar magnetic potential to describe the field behaviour, and the solution is determined by variables separation and boundary conditions. Also the accuracy of the proposed method is verified with FEM and some experimental results.

The purpose of this paper is to propose an analytical model to describe the magnetic field distribution in the air-gap of the QFA, which can quickly evaluate the scale factor of the QFA and help to design its torquer before it is manufactured. To our knowledge, it is the first time that an analytical method is used for magnetic field analysis in QFAs. The paper is organized as follows. Next section presents the structure of the magnetic circuit of the QFA, along with detailed theoretical analysis about the scalar magnetic potential equations and corresponding boundary conditions. Analytical solution is obtained through separating variables and then compared with FEM, and experimental results are followed to demonstrate the feasibility of the model. Conclusion section comes at last to summarize the whole article.

2. Analytical model

The working principle of the QFA is based on the flexible suspension of a gold coated pendulous reed attached with a pair of torque coils [29]. The serve control is fed with the position of the pendulous reed [30] and generates corresponding current in the torque coils, which are located in the magnetic field produced by the PM, to rebalance the pendulous reed and constitutes a closed loop system. The input acceleration can be obtained by measuring the current that flows through the torque coils [31,32].

The magnetic circuit structure of the model to analyse the magnetic flux density of the operation air-gap is shown in Fig. 1(a). Following assumptions are made to simplify the theoretical analysis:

- Iron yoke is infinitely permeable;
- Magnetic pole piece is utilized to redirect the magnetic flux from PM to a radially distributed field and is equivalently regarded as a PM with radial magnetization;
- The center of the slot arc differs from that of the air-gap or the pole piece, so the slot shape is simplified to a fan-shaped annular region (shown in the Fig. 1(b), concentric with others, but slightly larger than the original shape) for calculation convenience.

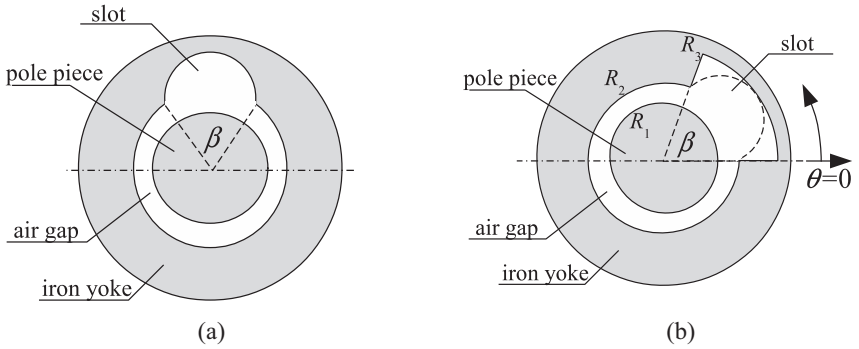

Fig. 1. Top view of magnetic circuit of QFA. (a) original structure; (b) simplified structure for calculation.

For calculation convenience, the polar coordinate is rotated clockwise by $(\frac{\pi}{2} - \frac{\beta}{2})$ in the analytical study to ensure the zero angle line coincides with the right side of the fan-shaped annular slot, which is also shown in Fig. 1(b). The whole structure is divided into slot (region 1, outer radius R_3), air-gap (region 2, outer radius R_2 and inner radiusR_1) and pole piece (region 3, outer radius R_1, assumed to be the PM region). In these regions, the magnetic flux density $\vec{B}$ and field intensity $\vec{H}$ are expressed as:

$$\text{In slot and air-gap region} \quad \vec{B} = \mu_0 \vec{H} \tag{1}$$

$$\text{In PM region} \quad \vec{B} = \mu_0 \mu_r \vec{H} + \mu_0 \vec{M} \tag{2}$$

where μ_0 is the permeability in vacuum and μ_r is the relative permeability of the PM. $\vec{M}$ is the residual magnetization vector. A magnetic scalar potential φ, whose minus gradient indicates magnetic field intensity $\vec{H}$, is utilized in 2-D polar coordinates to describe the problem, and the corresponding field behaviour can be governed by following Laplace or Poisson equations.

$$\text{In slot region} \quad \nabla^2 \varphi_1(r, \theta) = 0 \tag{3}$$

$$\text{In air-gap region} \quad \nabla^2 \varphi_2(r, \theta) = 0 \tag{4}$$

$$\text{In PM region} \quad \nabla^2 \varphi_3(r, \theta) = \frac{\nabla \cdot \vec{M}}{\mu_r} \tag{5}$$

where $\vec{M} = M_r \vec{r} + M_\theta \vec{\theta}$, $M_\theta = 0$. Considering radial magnetization assumption and Eq. (2),

$$M_r = \frac{B_r}{\mu_0} \tag{6}$$

with B_r representing the remanence of the PM.

Related boundary conditions can be summarized as following.

For the slot region.

$$\varphi_1(R_3, \theta) = 0 \quad 0 \leqslant \theta \leqslant \beta \tag{7}$$

$$\varphi_1(r, 0) = 0 \quad R_2 \leqslant r \leqslant R_3 \tag{8}$$

$$\varphi_1(r, \beta) = 0 \quad R_2 \leqslant r \leqslant R_3 \tag{9}$$

For the air-gap region.

$$\varphi_2(R_2,\theta)=\begin{cases}0 & \beta<\theta\leqslant 2\pi\\ \varphi_1(R_2,\theta) & 0\leqslant\theta\leqslant\beta\end{cases} \tag{10}$$

$$\frac{\partial\varphi_2(r,\theta)}{\partial r}\Big|_{r=R_2}=\frac{\partial\varphi_1(r,\theta)}{\partial r}\Big|_{r=R_2} \tag{11}$$

For the PM region.

$$\varphi_3(R_1,\theta)=\varphi_2(R_1,\theta) \tag{12}$$

$$\frac{\partial\varphi_3(r,\theta)}{\partial r}-\frac{\partial\varphi_2(r,\theta)}{\partial r}\Big|_{r=R_1}=\frac{M_r}{\mu_r} \tag{13}$$

By separating the variables r and θ, the general solutions of each region after substituting above boundary conditions can be expressed as following [33]. Additionally, the periodicity of the the scalar potential and the boundness of the field inside the PM are taken into consideration.

$$\varphi_1(r,\theta)=\sum_{k=1}^{\infty}\left[E_k\left(r^{-\frac{k\pi}{\beta}}-R_3^{-\frac{2k\pi}{\beta}}r^{\frac{k\pi}{\beta}}\right)\sin\left(\frac{k\pi}{\beta}\theta\right)\right] \tag{14}$$

$$\varphi_2(r,\theta)=A_0-\frac{M_r}{2\mu_r}R_1\ln r+\sum_{n=1}^{\infty}[(A_nr^{-n}+B_nr^n)\cos(n\theta)+(C_nr^{-n}+D_nr^n)\sin(n\theta)] \tag{15}$$

$$\varphi_3(r,\theta)=\underbrace{\frac{M_r}{2\mu_r}r(1+\cos\theta)}_{\text{special solution}}+M_0+\sum_{n=1}^{\infty}[r^n(M_n\cos(n\theta)+N_n\sin(n\theta))] \tag{16}$$

The first part of Eq. (16) is one special solution of Poisson Eq. (5), and the calculus of A_0 and M_0 is not necessary to compute the flux density expression. The coefficients A_n, B_n, C_n, D_n, M_n, N_n and E_k can be determined by Fourier series expansions over intervals $[0,2\pi]$ or $[0,\beta]$ [25]. A set of linear vector equations with regard to above coefficients and required to be solved is presented in the appendix, where N and K indicate the number of harmonic terms in the air-gap/PM region and the slot region.

The region of interest is the air-gap whose field distribution determines the electromagnetic force of the accelerometer, and the radial and tangential flux density can be derived as

$$B_r=-\mu_0\frac{\partial\varphi_2(r,\theta)}{\partial r} \tag{17}$$

$$B_\theta=-\frac{\mu_0}{r}\frac{\partial\varphi_2(r,\theta)}{\partial\theta} \tag{18}$$

3. Calculation results

In order to validate the proposed model, the analytical solutions are compared with FEM results obtained from ANSYS, whose model is established with the original structure and has no simplification. The parameters used for calculation are summarized in Table 1. In order to make analytical method and FEM results have the same polar coordinate, the coordinate of the analytical result is rotated back to the position depicted in Fig. 2.

Table 1
Parameters for calculation

Parameter	Value
R_1	4.6 mm
R_2	5.65 mm
R_3	8.75 mm
β	1.1819 rad
B_r	1.05 T
μ_r	1.1
N	20
K	20

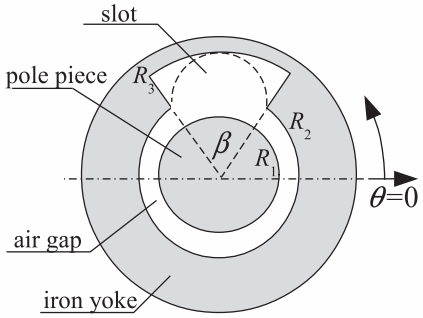

Fig. 2. Polor coordinate after rotating for comparison.

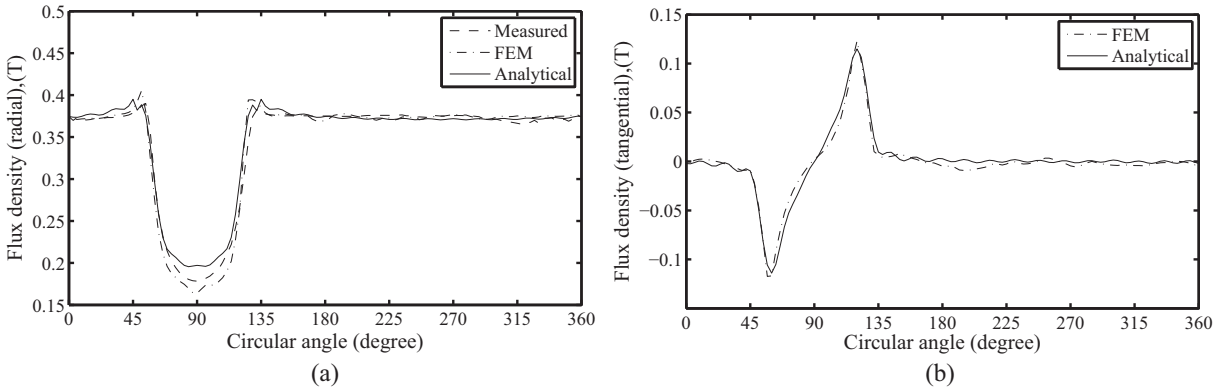

Fig. 3. Flux density distribution for radial component (a) and tangential component (b) in the middle of the air-gap (radius of 5.2 mm).

We have also implemented some measurements of the air-gap flux density by a portable Tesla meter (TGX-1000, 1% relative precision). Only the radial flux density was detected in the experiment due to the meter's probe with 3 mm width and 0.8 mm thickness, and it is impossible to rotate the sensitive direction of the probe in the extremely narrow air-gap region. The measured values and the calculated values of the radial flux density in the middle of the air-gap are plotted in Fig. 3, and only the calculated tangential values are presented considering the dimension limitation of the Tesla meter's probe. Distinct slot effect can be observed from these figures. The flux density distribution derived from the proposed model agrees well with that obtained from FEM and that measured from the actual air-gap except for little deviation in the slot opening area due to the existence of slot shape simplification. The steep curve variation around two slot borders of the radial flux density can be attributed to that the transitions from the air-gap to the slot have sharp corners resulting from discontinuity.

The relative deviations of the FEM and analytical results from the measured data are shown in Fig. 4, and most relative deviations are below 3% except those in the slot region, which validate the feasibility of the proposed analytical model.

The relation between the radial flux density and the air-gap radius is depicted in Fig. 5, and several radius values are selected from 4.95 mm to 5.45 mm, which indicate the inner and outer radius of the torque coil. Good agreement can also be observed from the figure, and θ under calculation is selected as 270° for example, similarly, the results of 0° or 180° shows no obvious difference with that of 270°.

Both the analytical model and the FEM are run on the the PC with dual-core 2.8 GHz CPU and

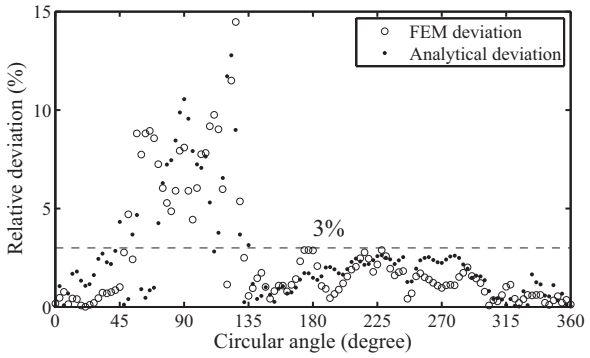

Fig. 4. Relative deviation of FEM method and analytical method.

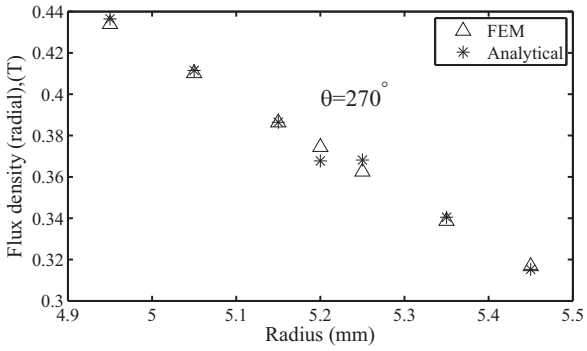

Fig. 5. Radial flux density distribution for different radius.

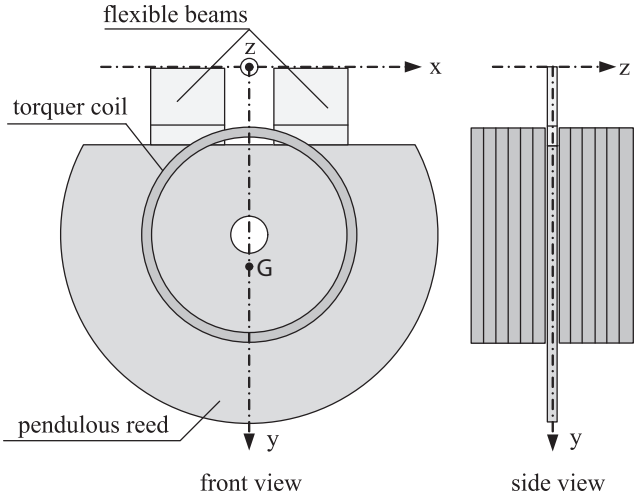

Fig. 6. Structure of pendulous components.

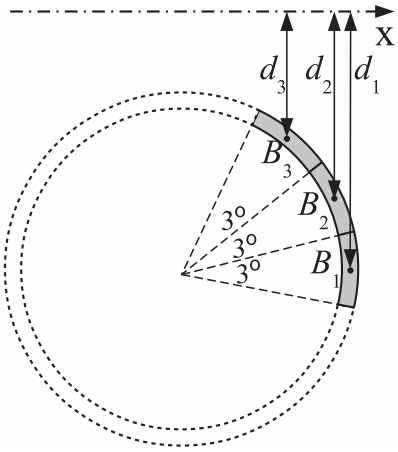

Fig. 7. Schematic of assumption for equilibrium calculation.

2 GB RAM, and the corresponding software are MATLAB R2011b and ANSYS 12.0 respectively. The elapsed calculation time of the analytical model is within 30 seconds, while the time cost to do FEM at least exceeds 1 hour. What is more, it is easy and flexible to adjust the parameters in the analytical model but the adjustment in the FEM requires redesigning structure and mesh, which is complex and time consuming. Therefore, this proposed analytical model exerts great superiority on rapid design and optimization of the accelerometer and other similar magnetic sensors.

In addition, we have assembled a quartz flexible accelerometer based on differential capacitance detection, and the above analytical solution can be employed to assess the performance of the rebalance electromagnetic force and predict the scale factor of the accelerometer. A pendulous reed attached with two torque coils constitutes a proof mass, whose structure with a rectangular coordinate is displayed in Fig. 6.

x axis is the pivot axis, and G is the gravity center of the proof mass, whose coordinate value is (0 mm, 8.833 mm, 0 mm) evaluated by Autodesk Inventor. The weight of the proof mass was measured to be 802.3 milligram (notated as m) by an electronic balance with 0.1 milligram precision. The number of windings of both coils reaches 290 (notated as n), and in the air-gap region, given that tangential

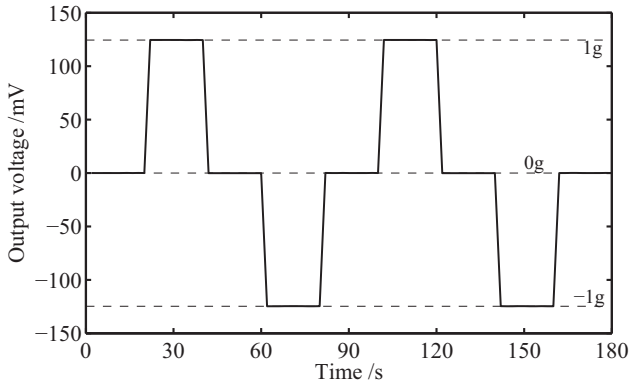

Fig. 8. Four position experiment results.

magnetic flux density's direction nearly accords with the winding direction of the lacquered wire and produces negligible force, two coils are suffered from a group of electromagnetic forces parallel to z axis induced only by radial flux density when current is injected according to the acceleration of the inertial frame. As plotted in Fig. 5, radial flux density almost decreases linearly with the radius in the coil region, so the flux density value at intermediate radius (5.2 mm) can be assumed to hold for all the radius. The analytical result in Fig. 3 has 120 data points during the interval $[0, 2\pi]$, and each point is assumed here to hold for a 3° coil segment. A schematic about above assumptions is presented in Fig. 7 for more clarity, where only 3 segments are shown as examples. Radial flux density in each segment B_i $(i = 1, 2, \ldots, 120)$ is considered constant and equals to that of the center point. d_i $(i = 1, 2, \ldots, 120)$ means y coordinate value of each center point, which is used to calculate the moment of electromagnetic force about x axis. If an acceleration of 1 g (9.8 m/s^2) is applied to the accelerometer, the corresponding current required to balance the proof mass indicates the scale factor, so equilibrium force and moment equations shown as following have to be satisfied.

$$\sum F_z = 0 \quad \left(\sum_{i=0}^{120} B_i I l n = mg \right) \tag{19}$$

$$\sum M_x = 0 \quad \left(\sum_{i=0}^{120} B_i I l n d_i = mgl_{\mathrm{g}} \right) \tag{20}$$

where l_{g} is the distance between the gravity center and x axis. The solution I of Eq. (19) is 1.208 mA, while the solution I of Eq. (20) is 1.284 mA. Strict equilibrium does not exist, therefore, the scale factor can be regarded to fall in the range [1.208 mA/g, 1.284 mA/g].

Of course, an experiment of the scale factor in the form of gravitational field roll-over test was followed to validate the effectiveness of above estimation. The QFA after assembly was mounted on a fixture and aligned on the dividing head with a precision 1″, where the input acceleration comes from the gravity projection. Four position experiment was implemented by rotating the dividing head clockwise at the position 0°, 90°, 180°, 270° and 360° in turn and then counter-clockwise. A high precision multimeter read 10 values from the sampling resistor (100 Ω) at each position, and the result are shown in Fig. 8. Four position experiment has good repetition and symmetry, and the scale factor of the improved QFA can be calculated as 1.246 mA/g, which is calculated as the half of the output current difference at 90° (1 g) and 270° (−1 g) and obviously belongs to the evaluated range.

4. Conclusion

In this paper, an analytical approach for calculating the air-gap magnetic field distribution in quartz flexible accelerometers has been developed. The Laplace and Poisson equations in polar coordinates have been solved by the technique of separation of variables and analysing boundary conditions in the slot, air-gap and PM domains. The model proposed in this work has been validated by finite element method and preliminary experiment, and can be used as an estimator of the rebalance performance and the scale factor. Therefore, this methodology is promising to serve as a design and optimization tool for quartz flexible accelerometers and other similar magnetic sensors.

Acknowledgments

This work was supported by the National Natural Science Foundation of China (Grant No. 51405340) and Foundation of State Key Laboratory of Precision Measuring Technology and Instruments (grant No. PIL1302).

Appendix A: Linear vector equations for determining the parameters of analytical solutions

The dot $\cdot$ in the following equations means the dot product of two vectors.

$$\begin{bmatrix} A_1 \\ A_2 \\ \vdots \\ A_N \end{bmatrix} \cdot \begin{bmatrix} R_1^{-1} \\ R_1^{-2} \\ \vdots \\ R_1^{-N} \end{bmatrix} + \begin{bmatrix} B_1 \\ B_2 \\ \vdots \\ B_N \end{bmatrix} \cdot \begin{bmatrix} R_1^{1} \\ R_1^{2} \\ \vdots \\ R_1^{N} \end{bmatrix} = \begin{bmatrix} M_1 \\ M_2 \\ \vdots \\ M_N \end{bmatrix} \cdot \begin{bmatrix} R_1^{1} \\ R_1^{2} \\ \vdots \\ R_1^{N} \end{bmatrix} + \begin{bmatrix} \dfrac{M_r}{2\mu_r} R_1 \\ 0 \\ \vdots \\ 0 \end{bmatrix} \tag{A.1}$$

$$\begin{bmatrix} C_1 \\ C_2 \\ \vdots \\ C_N \end{bmatrix} \cdot \begin{bmatrix} R_1^{-1} \\ R_1^{-2} \\ \vdots \\ R_1^{-N} \end{bmatrix} + \begin{bmatrix} D_1 \\ D_2 \\ \vdots \\ D_N \end{bmatrix} \cdot \begin{bmatrix} R_1^{1} \\ R_1^{2} \\ \vdots \\ R_1^{N} \end{bmatrix} = \begin{bmatrix} N_1 \\ N_2 \\ \vdots \\ N_N \end{bmatrix} \cdot \begin{bmatrix} R_1^{1} \\ R_1^{2} \\ \vdots \\ R_1^{N} \end{bmatrix} \tag{A.2}$$

$$\begin{bmatrix} A_1 \\ A_2 \\ \vdots \\ A_N \end{bmatrix} \cdot \begin{bmatrix} -R_1^{-2} \\ -R_1^{-3} \\ \vdots \\ -R_1^{-N-1} \end{bmatrix} + \begin{bmatrix} B_1 \\ B_2 \\ \vdots \\ B_N \end{bmatrix} \cdot \begin{bmatrix} R_1^{0} \\ R_1^{1} \\ \vdots \\ R_1^{N-1} \end{bmatrix} = \begin{bmatrix} M_1 \\ M_2 \\ \vdots \\ M_N \end{bmatrix} \cdot \begin{bmatrix} R_1^{0} \\ R_1^{1} \\ \vdots \\ R_1^{N-1} \end{bmatrix} + \begin{bmatrix} \dfrac{M_r}{2\mu_r} \\ 0 \\ \vdots \\ 0 \end{bmatrix} \tag{A.3}$$

$$\begin{bmatrix} C_1 \\ C_2 \\ \vdots \\ C_N \end{bmatrix} \cdot \begin{bmatrix} -R_1^{-2} \\ -R_1^{-3} \\ \vdots \\ -R_1^{-N-1} \end{bmatrix} + \begin{bmatrix} D_1 \\ D_2 \\ \vdots \\ D_N \end{bmatrix} \cdot \begin{bmatrix} R_1^{0} \\ R_1^{1} \\ \vdots \\ R_1^{N-1} \end{bmatrix} = \begin{bmatrix} N_1 \\ N_2 \\ \vdots \\ N_N \end{bmatrix} \cdot \begin{bmatrix} R_1^{0} \\ R_1^{1} \\ \vdots \\ R_1^{N-1} \end{bmatrix} \tag{A.4}$$

$$\begin{bmatrix} A_1 \\ A_2 \\ \vdots \\ A_N \end{bmatrix} \cdot \begin{bmatrix} R_2^{-1} \\ R_2^{-2} \\ \vdots \\ R_2^{-N} \end{bmatrix} + \begin{bmatrix} B_1 \\ B_2 \\ \vdots \\ B_N \end{bmatrix} \cdot \begin{bmatrix} R_2^{1} \\ R_2^{2} \\ \vdots \\ R_2^{N} \end{bmatrix} = \frac{1}{\pi} F^T \begin{bmatrix} A_1 \\ A_2 \\ \vdots \\ A_K \end{bmatrix} \cdot \begin{bmatrix} R_2^{\frac{-\pi}{\beta}} - R_3^{\frac{-2\pi}{\beta}} R_2^{\frac{\pi}{\beta}} \\ R_2^{\frac{-2\pi}{\beta}} - R_3^{\frac{-4\pi}{\beta}} R_2^{\frac{2\pi}{\beta}} \\ \vdots \\ R_2^{\frac{-K\pi}{\beta}} - R_3^{\frac{-2\,K\pi}{\beta}} R_2^{\frac{K\pi}{\beta}} \end{bmatrix} \tag{A.5}$$

$$\begin{bmatrix} C_1 \\ C_2 \\ \vdots \\ C_N \end{bmatrix} \cdot \begin{bmatrix} R_2^{-1} \\ R_2^{-2} \\ \vdots \\ R_2^{-N} \end{bmatrix} + \begin{bmatrix} D_1 \\ D_2 \\ \vdots \\ D_N \end{bmatrix} \cdot \begin{bmatrix} R_2^{1} \\ R_2^{2} \\ \vdots \\ R_2^{N} \end{bmatrix} = \frac{1}{\pi} G^T \begin{bmatrix} A_1 \\ A_2 \\ \vdots \\ A_K \end{bmatrix} \cdot \begin{bmatrix} R_2^{\frac{-\pi}{\beta}} - R_3^{\frac{-2\pi}{\beta}} R_2^{\frac{\pi}{\beta}} \\ R_2^{\frac{-2\pi}{\beta}} - R_3^{\frac{-4\pi}{\beta}} R_2^{\frac{2\pi}{\beta}} \\ \vdots \\ R_2^{\frac{-K\pi}{\beta}} - R_3^{\frac{-2K\pi}{\beta}} R_2^{\frac{K\pi}{\beta}} \end{bmatrix} \tag{A.6}$$

$$\begin{aligned} &\frac{\beta}{2} \begin{bmatrix} A_1 \\ A_2 \\ \vdots \\ A_K \end{bmatrix} \cdot \begin{bmatrix} \frac{\pi}{\beta} \\ \frac{2\pi}{\beta} \\ \vdots \\ \frac{K\pi}{\beta} \end{bmatrix} \cdot \begin{bmatrix} -R_2^{\frac{-\pi}{\beta}-1} - R_3^{\frac{-2\pi}{\beta}} R_2^{\frac{\pi}{\beta}-1} \\ -R_2^{\frac{-2\pi}{\beta}-1} - R_3^{\frac{-4\pi}{\beta}} R_2^{\frac{2\pi}{\beta}-1} \\ \vdots \\ -R_2^{\frac{-K\pi}{\beta}-1} - R_3^{\frac{-2\,K\pi}{\beta}} R_2^{\frac{K\pi}{\beta}-1} \end{bmatrix} = H+ \\ &F \begin{bmatrix} 1 \\ 2 \\ \vdots \\ N \end{bmatrix} \cdot \left\{ \begin{bmatrix} -A_1 \\ -A_2 \\ \vdots \\ -A_N \end{bmatrix} \cdot \begin{bmatrix} R_2^{-2} \\ R_2^{-3} \\ \vdots \\ R_2^{-N-1} \end{bmatrix} + \begin{bmatrix} B_1 \\ B_2 \\ \vdots \\ B_N \end{bmatrix} \cdot \begin{bmatrix} R_2^{0} \\ R_2^{1} \\ \vdots \\ R_2^{N-1} \end{bmatrix} \right\} + \\ &G \begin{bmatrix} 1 \\ 2 \\ \vdots \\ N \end{bmatrix} \cdot \left\{ \begin{bmatrix} -C_1 \\ -C_2 \\ \vdots \\ -C_N \end{bmatrix} \cdot \begin{bmatrix} R_2^{-2} \\ R_2^{-3} \\ \vdots \\ R_2^{-N-1} \end{bmatrix} + \begin{bmatrix} D_1 \\ D_2 \\ \vdots \\ D_N \end{bmatrix} \cdot \begin{bmatrix} R_2^{0} \\ R_2^{1} \\ \vdots \\ R_2^{N-1} \end{bmatrix} \right\} \end{aligned} \tag{A.7}$$

where the elements of matrices F and G and vector H are expressed as

$$F(k,n) = \int_0^{\beta} \sin\left(\frac{k\pi}{\beta}\theta\right) \cos(n\theta) d\theta = \frac{-kn\beta[(-1)^k \cos(n\beta) - 1]}{k^2\pi^2 - n^2\beta^2} \tag{A.8}$$

$$G(k,n) = \int_0^{\beta} \sin\left(\frac{k\pi}{\beta}\theta\right) \sin(n\theta) d\theta = \frac{-kn\beta(-1)^k \sin(n\beta)}{k^2\pi^2 - n^2\beta^2} \tag{A.9}$$

$$H(k) = \int_0^{\beta} -\frac{M_r R_1}{2\mu_r R_2} \sin\left(\frac{k\pi}{\beta}\theta\right) d\theta = \frac{M_r R_1 \beta}{2\mu_r R_2\, k\pi}[(-1)^k - 1] \tag{A.10}$$

References

[1] J.L. Weston and D.H. Titterton, Modern inertial navigation technology and its application, *Electronics & Communication Engineering Journal* **12** (2000), 49–64.

[2] V.F. Strachan, Inertial measurement technology in the satellite navigation environment, *Journal of Navigation* **53** (2000), 247–260. doi: http://dx.doi.org/.
[3] M.S. Grewal, L.R. Weill and A.P. Andrews, Global positioning systems, inertial navigation, and integration, John Wiley & Sons, 2007.
[4] N.M. Barbour, Inertial navigation sensors, Charles Stark Draper Lab Inc Cambridge MA, 2010.
[5] R. Cao, Y. Chen and R. Kang, Failure mechanism analysis of quartz accelerometer under vibration condition, in: *Prognostics and System Health Management Conference (PHM-Shenzhen), 2011*, IEEE, (2011), 1–5. doi: 10.1109/PHM.2011.5939506.
[6] W.S. Che and J.H. Oh, Development of force-balance accelerometer with high accuracy for precision motion measurement, *Measurement Science and Technology* **7** (1996), 1001–1011.
[7] E.D. Jacobs, Accelerometer, US Patent, 1972.
[8] R.C. Mehta, The development of accelerometers, *Electronics & Power* **11** (1965), 304–307. doi: 101049/ep.1965.0227.
[9] A. Lawrence and A. Lawrence, Modern inertial technology, Springer, 1998.
[10] C. Wang, X. Li, K. Kou, T. Wu and C. Long, Optimization of magnetic hat for quartz flexible accelerometer, *Sensor Review* **36** (2016). doi: 101108/SR-04-2015-0067.
[11] X.D. Yu, J.L. Li, S.K. Yan, G. Wei and G. Li, Temperature drift compensation based on artificial fish swarm algorithm for quartz flexible accelerometer, *Applied Mechanics and Materials* **513** (2014), 4030–4034. doi: 10.4028/www.scientific.net/AMM513-517.4030.
[12] S.L. Mu, F.B. Chen, J.M. Gao and Z.Z. Wu, Research on temperature compensation method of quartz flexible accelerometer, *Applied Mechanics and Materials* **423** (2013), 2308–2312. doi: 104028/www.scientific.net/AMM.423-426.2308.
[13] Y. Chen, B. Liu, R. Kang and Z. Hou, Study on parameter drift mechanism of a quartz accelerometer with a system analysis method, *Chemical Engineering* **33** (2013), 13–18.
[14] C. Zhao, X. Zhong, Q. Dang and L. Zhao, De-noising signal of the quartz flexural accelerometer by multiwavelet shrinkage, *International Journal on Smart Sensing and Intelligent Systems* **6** (2013), 191–208.
[15] Y. Chen, B. Liu, Z. Hou and R. Kang, Simulation of residual stress in laser welding of quartz flexible accelerometer, in: *2012 IEEE Conference on Prognostics and System Health Management (PHM)*, IEEE, (2012), 1–5. doi: 10.1109/PHM.20126228916.
[16] G. Filippopoulos and D. Tsanakas, Analytical calculation of the magnetic field produced by electric power lines, *IEEE Transactions on Power Delivery* **20** (2005), 1474–1482. doi: 101109/TPWRD.2004.839184.
[17] R. Ravaud, G. Lemarquand and V. Lemarquand, Magnetic field created by tile permanent magnets, *IEEE Transactions on Magnetics* **45** (2009), 2920–2926. doi: 101109/TMAG.2009.2014752.
[18] L. Jian and K.-T. Chau, Analytical calculation of magnetic field distribution in coaxial magnetic gears, *Progress in Electromagnetics Research* **92** (2009), 1–16. doi: 102528/PIER09032301.
[19] H.A. Leupold and E. Potenziani, An overview of modern permanent magnet design, Army Lab Command Fort Monmouth NJ Electronics Technology and Devices Lab, 1990.
[20] H.A. Leupold, Approaches to permanent magnet circuit design, *IEEE Transactions on Magnetics* **29** (1993), 2341–2346. doi: 101109/20.280860.
[21] L. Huang, G. Zhao, H. Nian and Y. He, Modeling and design of permanent magnet biased radial-axial magnetic bearing by extended circuit theory, in: *2007 International Conference on Electrical Machines and Systems*, IEEE, (2007), 1502–1507.
[22] Z.Q. Zhu, D. Howe and C.C. Chan, Improved analytical model for predicting the magnetic field distribution in brushless permanent-magnet machines, *IEEE Transactions on Magnetics* **38** (2002), 229–238. doi: 101109/20.990112.
[23] Z.P. Xia, Z.Q. Zhu and D. Howe, Analytical magnetic field analysis of halbach magnetized permanent-magnet machines, *IEEE Transactions on Magnetics* **40** (2004), 1864–1872. doi: 101109/TMAG.2004.828933.
[24] Z.J. Liu and J.T. Li, Analytical solution of air-gap field in permanent-magnet motors taking into account the effect of pole transition over slots, *IEEE Transactions on Magnetics* **43** (2007), 3872–3883. doi: 101109/TMAG.2007.903417.
[25] T. Lubin, S. Mezani and A. Rezzoug, Exact analytical method for magnetic field computation in the air gap of cylindrical electrical machines considering slotting effects, *IEEE Transactions on Magnetics* **46** (2010), 1092–1099. doi: 10.1109/TMAG2009.2036257.
[26] L. Jian, G. Xu, C.C. Mi, K.T. Chau and C.C. Chan, Analytical method for magnetic field calculation in a low-speed permanent-magnet harmonic machine, *IEEE Transactions on Energy Conversion* **26** (2011), 862–870. doi: 10.1109/TEC2011.2140373.
[27] S.I. Bekinal, T.R. Rao Anil and S. Jana, Analysis of the magnetic field created by permanent magnet rings in permanent magnet bearings, *International Journal of Applied Electromagnetics and Mechanics* **46** (2014), 255–269. doi: 10.3233/JAE-141776.
[28] L. Tian, Y. Tian, Q. Tian and R. Jia, Magnetic force analytic model of step conical PMB, *International Journal of Applied Electromagnetics and Mechanics* **47** (2015), 293–304. doi: 103233/JAE-130130.
[29] T. Usuda, C. Weißenborn and H.J.V. Martens, Theoretical and experimental investigation of transverse sensitivity of

accelerometers under multiaxial excitation, *Measurement Science and Technology* **15** (2004), 896–904.
[30] V. Josselin, P. Touboul and R. Kielbasa, Capacitive detection scheme for space accelerometers applications, *Sensors and Actuators A: Physical* **78** (1999), 92–98. doi: 101016/S0924-4247(99)00227-7.
[31] L. Li, C. Zhang, X. Zhang, W. Xu and C. Li, Investigation on noise of digital close-loop Q-flex accelerometer, in: *2011 6th IEEE Conference on Industrial Electronics and Applications*, IEEE, (2011), 614–619. doi: 10.1109/ICIEA.2011.5975659.
[32] S. Zhang, X. Zhang and D. Li, Accuracy analysis of digital closed-loop quartz flex accelerometer based on differential capacitance detection technology, in: *2013 International Conference on Computational and Information Sciences*, IEEE, (2013), 191–194. doi: 101109/ICCIS.2013.58.
[33] S.J. Farlow, Partial differential equations for scientists and engineers, Courier Dover Publications, 2012.